Emergent antiferromagnetism in Y-shaped Kekulé graphene

Chenyue Wen,[1,2] Wanpeng Han,[1] Xukun Feng,[3] Xingchuan Zhu,[4] Weisheng Zhao,[2] Shengyuan A. Yang,[3] Shiping Feng,[5] and Huaiming Guo[1,*]

[1]*School of Physics, Beihang University, Beijing, 100191, China*

[2]*Fert Beijing Institute, MIIT Key Laboratory of Spintronics, School of Integrated Circuit Science and Engineering, Beihang University, Beijing 100191, China*

[3]*Research Laboratory for Quantum Materials, Singapore University of Technology and Design, Singapore 487372, Singapore*

[4]*Interdisciplinary Center for Fundamental and Frontier Sciences, Nanjing University of Science and Technology, Jiangyin, Jiangsu 214443, P. R. China*

[5]*Department of Physics, Beijing Normal University, Beijing, 100875, China*

(Received 16 September 2022; revised 23 November 2022; accepted 30 November 2022; published 12 December 2022)

Antiferromagnetic (AFM) transitions of birefringent Dirac fermions created by a Y-shaped Kekulé distortion in graphene are investigated by mean-field theory and determinant quantum Monte Carlo simulations. We show that the quantum critical point can be continuously tuned by the bond-modulation strength, and the universality of the quantum criticality remains in the Gross-Neveu-Heisenberg class. The critical interaction scales with the geometric average of the two velocities of the birefringent Dirac cones, and decreases monotonically between the uniform and completely depleted limits. Since the AFM critical interaction can be tuned to very small values, antiferromagnetism may emerge automatically, realizing the long-sought magnetism in graphene. These results enrich our understanding of the semimetal-AFM transitions in Dirac-fermion systems, and open a route to achieve magnetism in graphene.

DOI: 10.1103/PhysRevB.106.245116

I. INTRODUCTION

Graphene features linear dispersions near the Fermi energy [1,2], which is described by a massless Dirac equation. The electrons therein are thus called Dirac fermions, which have been the origin of various exotic properties [3–5]. While theoretical studies have suggested abundant topological or ordered phases in graphene, as generated by various kinds of mechanisms [6–12], their experimental observations are lacking due to the overall weak correlation effects in graphene.

Achieving magnetism in graphene is actively pursued in the hope of its spintronic applications. Although pristine graphene has a nonmagnetic ground state, magnetic orders have been observed at the zigzag edges, defects, and hydrogen-terminated vacancies [13–22]. The emergent magnetism is generally related to the associated localized states [23], for which the correlation effect is greatly enhanced, resulting in magnetic ordering at much weaker interactions [24–26]. From this physical mechanism, it is clear that the above magnetisms are restricted to specific regions of graphene, e.g., edges or defects. Inducing a robust long-range magnetic order in the bulk of graphene remains a challenge.

In this paper, we propose that the Y-shaped Kekulé distortion can induce a global antiferromagnetic (AFM) order in graphene. Our paper is motivated by recent experiments which successfully realized such distortion in graphene grown on Cu(111) with regular surface copper vacancies [27] and on transition-metal dichalcogenide substrates [28]. We show that the Y-shaped bond texture modifies the Fermi velocities of two pairs of low-energy bands differently, creating birefringent Dirac fermions. AFM transitions of such fermions are investigated by two complementary methods: mean-field theory and large-scale determinant quantum Monte Carlo (DQMC) simulations. Both methods predict a semimetal (SM)-AFM transition and find that the critical interaction is proportional to the geometric average of the two velocities of birefringent Dirac fermions. The DQMC simulations quantitatively determine the critical values using finite-size scaling. In addition, it is found that the quantum criticality remains in the Gross-Neveu-Heisenberg universality class. Our results show that the Y-shaped distortion enables an additional degree of control of Dirac fermions, and provides a way to tune the quantum critical point. Importantly, we reveal that when the distortion strength is large enough, the critical interaction may be well below the actual value of U/t in graphene [29,30], generating global AFM long-range order. Considering the recent progress in engineering the Y-shaped Kekulé distortion [27,28], our result provides a feasible approach to realize magnetic graphene in experiment.

II. MODEL

Our paper is based on the Hubbard model defined on a honeycomb lattice with a Y-shaped Kekulé distortion,

$$H = -\sum_{\langle ij\rangle\sigma} t_{ij}(c^{\dagger}_{i\sigma}c_{j\sigma} + \text{H.c.}) + U\sum_{i} n_{i\uparrow}n_{i\downarrow}, \qquad (1)$$

*hmguo@buaa.edu.cn

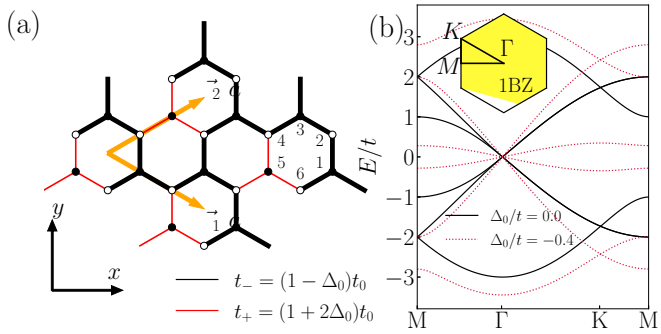

FIG. 1. (a) Honeycomb lattice with a Y-shaped bond modulation. Black and white dots label the two sublattices, and black and red lines distinguish different bond strengths. The different sites in the unit cell are marked by a set of integers $(1-6)$. (b) The energy spectrum along the high-symmetry directions of the Brillouin zone at $\Delta_0/t = 0$ and -0.4. Inset of (b) is the first Brillouin zone with the high-symmetry points labeled.

where $c^\dagger_{i\sigma}$ and $c_{i\sigma}$ are the creation and annihilation operators, respectively, at site i with spin $\sigma = \uparrow, \downarrow$; $\langle ij\rangle$ denotes nearest neighbors; $n_{i\sigma} = c^\dagger_{i\sigma}c_{i\sigma}$ is the number operator of electrons; and U is the on-site repulsion. Due to the Y-shaped modulation, the hopping amplitudes are modified as $t_{ij} = (1+2\Delta_0)t$ or $(1-\Delta_0)t$, depending on the position and direction of the bond [see Fig. 1(a)], where $\Delta_0 \in [-0.5, 1]$. The modifications are defined in such a way to keep the total bandwidth more or less unchanged. The pristine honeycomb lattice is restored at $\Delta_0 = 0$. In the limit $\Delta_0 = -0.5$, the fifth site in each unit cell is completely isolated from the lattice [see Fig. 1(a)], generating a $1/6$-depleted honeycomb lattice. This is similar to the Lieb lattice (also known as $1/4$-depleted square lattice) [31]. $\Delta_0 > 0$ interchanges the strong and weak bonds as in the $\Delta_0 < 0$ case, and the lattice is completely broken into isolated four-site stars at $\Delta_0 = 1$.

Under the Y-shaped distortion, the lattice has a six-site unit cell [see Fig. 1(a)]. Let's first neglect the interaction term in Eq. (1), then the electronic band structure contains six dispersive bands, as shown in Fig. 1(b). By a Brillouin zone (BZ) folding process, the bands of the $\Delta_0 = 0$ case in such a plot can be obtained from the pristine graphene band structure, where the two inequivalent Dirac points at the corners of the BZ are folded to the Γ point and the Dirac cones will coincide. For $\Delta_0 \neq 0$, although the linear dispersions remain near the Dirac points, the Dirac cone degeneracy is lifted, generating birefringent Dirac fermions with two different Fermi velocities, as in Fig. 1(b). By projecting the full Hamiltonian to the low-energy space at Γ, an effective Hamiltonian can be deduced (see Appendix A). The energy spectrum contains four branches with $E = \pm\frac{3}{2}(1-\Delta_0)tk$ and $E = \pm\frac{3}{2}\alpha(1-\Delta_0)tk$, with $\alpha = \frac{1+2\Delta_0}{\sqrt{1+2\Delta_0^2}}$. The two Fermi velocities are, respectively, given by (see also Fig. 7 in Appendix A)

$$v_1 = \tfrac{3}{2}(1-\Delta_0)t, \quad v_2 = \tfrac{3}{2}\alpha(1-\Delta_0)t. \tag{2}$$

It is noted that v_2 becomes zero in two limits: $\Delta_0 = -0.5$ or 1, generating two or four flat bands at the Fermi energy. When Δ_0 approaches the above two limits, the low-energy bands will be flattened, and the corresponding states tend to localize on the sites connected by the weakened bonds. Then, the correlation effect in the low-energy bands will be enhanced, and we expect that the AFM critical interaction will be significantly reduced. This expectation will be explored by two theoretical approaches, as we demonstrate below.

III. MEAN-FIELD THEORY APPROACH

Within the mean-field approximation, the interacting term $Un_{i\uparrow}n_{i\downarrow}$ is decoupled in the density channel as [32–34] $n_{i\uparrow}n_{i\downarrow} \approx n_{i\uparrow}\langle n_{i\downarrow}\rangle + \langle n_{i\uparrow}\rangle n_{i\downarrow} - \langle n_{i\uparrow}\rangle\langle n_{i\downarrow}\rangle$. To incorporate the possible AFM order, the averages of the operators are written as

$$\langle n_{i\uparrow(\downarrow)}\rangle = \tfrac{1}{2} \pm \rho_i, \quad \text{for } i \in \{1,3,5\}, \tag{3}$$

and

$$\langle n_{i\uparrow(\downarrow)}\rangle = \tfrac{1}{2} \mp \rho_i, \quad \text{for } i \in \{2,4,6\}, \tag{4}$$

with ρ_i being the order parameters, where i labels the six sites in a unit cell. We consider equal number of spin-up and spin-down electrons, such that the following restriction applies on the six order parameters: $\rho_1 + \rho_3 + \rho_5 = \rho_2 + \rho_4 + \rho_6$, which means only five of them are independent.

In the momentum space, the mean-field Hamiltonian is then

$$H_{\rm MF} = \sum_{\boldsymbol{k}\sigma} \psi^\dagger_{\boldsymbol{k}\sigma}\mathcal{H}^\sigma(\boldsymbol{k})\psi_{\boldsymbol{k}\sigma} + E_0, \tag{5}$$

with

$$\mathcal{H}^\sigma(\boldsymbol{k}) = \begin{pmatrix} h^\sigma_{11} & h_{12}(\boldsymbol{k}) \\ h^\dagger_{12}(\boldsymbol{k}) & h^\sigma_{22} \end{pmatrix}, \tag{6}$$

where $\psi_{\boldsymbol{k}\sigma} = (c_{1,\boldsymbol{k}\sigma}, \cdots, c_{6,\boldsymbol{k}\sigma})^T$ is a six-element basis, $h^\sigma_{11} = \mp\mathrm{diag}(\rho_1, \rho_3, \rho_5)$, $h^\sigma_{22} = \pm\mathrm{diag}(\rho_2, \rho_4, \rho_6)$, and the constant $E_0 = NU/4 + NU\sum_{i=1}^6 \rho_i^2/6$ with N the total number of sites. The order parameters ρ_i in the ground state can be calculated by minimizing the total energy from the mean field Hamiltonian.

Although the order parameters ρ_i are generally different within the unit cell due to the inhomogeneous bond textures, their curves as a function of U have the same features. Hence, we use their arithmetic mean, $\overline{\rho} = \frac{1}{6}\sum_{i=1}^6 \rho_i$, to characterize the AFM transition. Figure 2(a) shows $\overline{\rho}$ as a function of U for various values of Δ_0 at zero temperature. The values of $\overline{\rho}$ keep almost zero at weak interactions, and the system is in the semimetal phase. After passing a critical interaction U_c, $\overline{\rho}$ becomes finite, and increases rapidly with U, suggesting the AFM order develops in the system. As the absolute value of Δ_0 increases, the curves move leftward, indicating that the critical interaction decreases monotonically with increasing Δ_0.

Since the curves of $\overline{\rho}$ are continuous, it is not straightforward to determine U_c. Here, we use the critical slowing down at the phase transition to determine U_c. Specifically, the self-consistent process becomes the slowest at the transition point, which is reflected in the maximum cycling time n_c to get convergent self-consistent results. We checked that the critical value at $\Delta_0 = 0$ obtained by this method is in good agreement with the previous study [35]. Our result is shown in Fig. 3.

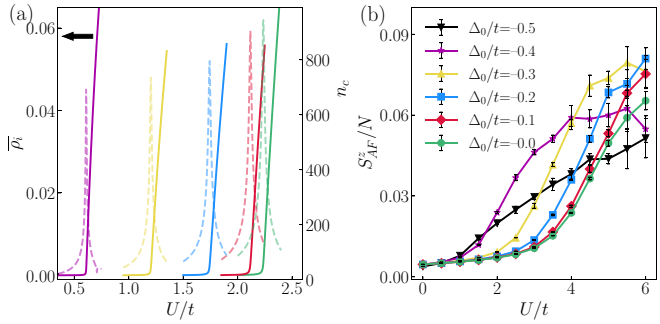

FIG. 2. (a) The mean-field order parameter and the cycling time n_c to get convergent solution in the self-consistent process as a function of U for various values of Δ_0. The sharp peak in the n_c curve can steadily determine the transition point. (b) The AFM structure factor obtained by DQMC as a function of U on a lattice with the size $L = 6$.

One finds that the critical interaction of the semimetal-AFM transition decreases monotonically from $U_c/t = 2.23$ at $\Delta_0 = 0$ to $U_c/t = 0$ at $\Delta_0 = -0.5$. Similarly, U_c also decreases monotonically with Δ_0 for $\Delta_0 > 0$ (see Appendix C).

IV. DQMC APPROACH

In the DQMC approach, Eq. (1) at finite interactions is solved numerically, where one decouples the on-site interaction term through the introduction of an auxiliary Hubbard-Stratonovich field, which is then integrated out stochastically [36–39]. The only errors are those associated with the statistical sampling, the finite spatial lattice size, and the inverse temperature discretization. These errors can be well controlled in the sense that they can be systematically reduced as needed and further eliminated by appropriate extrapolations. At half filling, the simulation is free of the sign problem, due to the presence of particle-hole symmetry [40–43]. Thus we can access low enough temperatures,

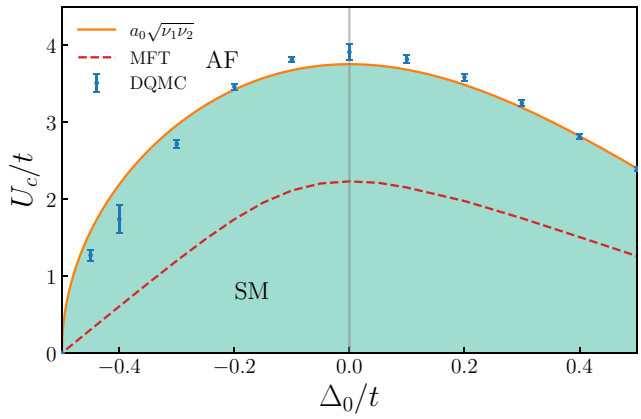

FIG. 3. The phase diagram in the (Δ_0, U_c) plane. The dashed line represents the mean-field boundary, which underestimates the critical interaction. The DQMC critical values can be well fitted using the ansatz $U_c = a_0\sqrt{\nu_1\nu_2}$, implying the critical interaction is proportional to the geometric average of the two velocities of the Dirac cones.

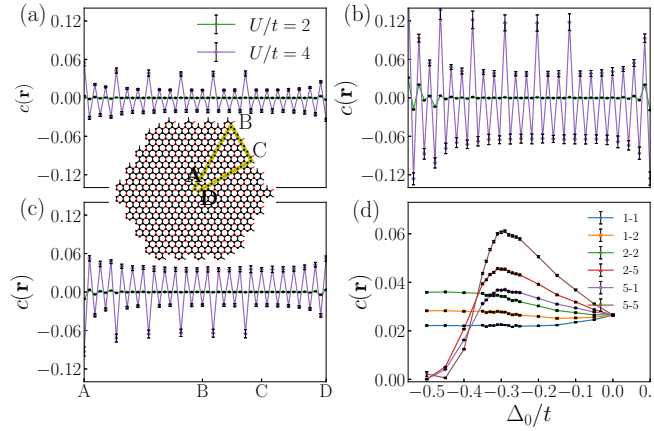

FIG. 4. The spin correlations along the high-symmetry paths [see inset of (a) and (c)]. The origin is placed on the (a) first, (b) second, and (c) fifth sites of the unit cell at (0, 0), which are representatives of the different ones in the unit cell. Here the anisotropic parameter is $\Delta_0/t = -0.3$. (d) The spin-spin correlations as a function of Δ_0 for the largest distance on a $L = 20$ lattice in the large-U limit.

necessary to determine the ground-state properties on finite-size lattices. In our calculation, we use the inverse temperature $\beta = 20$ and its discretization $\Delta\tau = 0.1$. The lattice has totally $N = 6 \times L \times L$ sites, with L up to 8.

Applying DQMC to our problem, the AFM order is characterized by the staggered structure factor [44] with

$$S^z_{\mathrm{AFM}} = \frac{1}{N}\sum_{i,j} \mathrm{sgn}(i,j)\langle S^z_i S^z_j\rangle, \tag{7}$$

where $\mathrm{sgn}(i, j) = +(-)$ when i, j belong to the same (opposite) sublattice. Since the Hubbard model in Eq. (1) preserves the spin SU(2) symmetry, the spin-spin correlations of the three spin components are identical, and we only consider the z component here. A related physical quantity of interest here is the sublattice magnetization, which is given by $m_s = \sqrt{S^z_{\mathrm{AFM}}/N}$.

Figure 2(b) shows calculated m_s^2 as a function of U on a $L = 6$ lattice for various negative values of Δ_0. At $\Delta_0 = 0$, it is known that AFM order exists when U exceeds $U_c = 3.86$ [45–51]. In the $\Delta_0 = -0.5$ limit, the geometry corresponds to the 1/6-depleted honeycomb lattice, where AFM order is expected to exist for all $U > 0$ due to the existence of flat band. The behavior of m_s^2 versus U is qualitatively similar for different values of Δ_0: m_s^2 increases continuously with U, thus the semimetal-AFM transition is of second-order nature. In addition, as Δ_0 increases, the curves shift to the weak-interaction side, which results from the decrease of the critical interaction U_c as the absolute value of Δ_0 increases. These confirm the observation from the mean field approach.

To gain additional insight into the behavior of AFM order, it is useful to examine the equal-time real space spin-spin correlation function $c(\boldsymbol{r}) = \langle(n_{j+\boldsymbol{r}\uparrow} - n_{j+\boldsymbol{r}\downarrow})(n_{j\uparrow} - n_{j\downarrow})\rangle$. Figure 4 shows $c(\boldsymbol{r})$ for $\Delta_0 = -0.3$ at $U/t = 2, 4$ on a $L = 6$ lattice. The origin is placed on the first site of the unit cell at (0, 0), and $\boldsymbol{r}$ runs along a triangular path [see Fig. 4(a)]. Since $U/t = 2$ is below the critical interaction ($U_c/t = 2.85$, see the following finite-size scaling), the values of the

TABLE I. The ratio between U_c and the averaged velocity in the literature. $\alpha = \sqrt{V_{\rm BZ}/(2\pi N_{\rm Dirac})}$ in Refs. [48,52] with $V_{\rm BZ} = \frac{8\pi^2}{3\sqrt{3}}(2\pi^2)$ and $N_{\rm Dirac} = 2$, which compensates the difference among the models in the linear part of the density of states. Δ in Ref. [52] is the pairing amplitude in the square-lattice Hubbard model with a d-wave pairing.

Honeycomb	π-flux	d-wave SC [52]
$U_c/\sqrt{v_1 v_2} \simeq 2.54$[50]	$\simeq$2.42[50]	$U_c/\sqrt{\alpha\bar{v}} \simeq 2.15$ ($\Delta = 1$)
$U_c/\sqrt{\alpha v_F^0} \simeq 2.33$[48]	$\simeq$2.21[48]	$U_c/\sqrt{\alpha\bar{v}} \simeq 2.19$ ($\Delta = 0.5$)

correlation at large distance are almost zero. On the other hand, the correlation length becomes comparable to the system size for the case of $U/t = 4$. $c(\boldsymbol{r})$ has a robust persistence at large distance, and its sign is consistent with AFM order. This behavior is consistent with the fact that $U/t = 4$ is above the critical point, and there exists AFM order in the system. The sites in the lattice can be classified into three categories according to the number of the weakened bonds connected. $c(\boldsymbol{r})$ varies among the different kinds of pairs of sites, which is most pronounced in the large-U limit. As shown in Fig. 4(d), it increases with the total number of weakened bonds connected to the two sites in each pair, exhibiting an interesting behavior: The less the site is connected to the lattice, the stronger it is correlated to other sites.

The behavior of $S^z_{\rm AFM}$ indicates that AFM order may develop at a decreased critical interaction in the presence of Y-shaped bond modulation in going from the pristine honeycomb lattice to the limiting cases of $\Delta_0 = -0.5, 1$. We then use finite-size scaling to analyze quantitatively the position of the critical point in the thermodynamic limit. The square of the order parameter is given by $S^z_{\rm AFM}/N$ in the $1/L \to 0$ limit. These extrapolated values are shown in the phase diagram Fig. 3. As a function of Δ_0, the critical interaction strength continuously decreases from $U_c/t = 3.869$ to zero. In addition, we use the ansatz $U_c = a_0\sqrt{v_1 v_2}$ to fit the boundary and find that the critical values are well fitted with $a_0 = 2.51$. This verifies the conjecture that the critical interaction is proportional to the geometric average of the two velocities of birefringent Dirac fermions. We list the ratios reported in the existing studies in Table I, which is consistent with the value ($a_0 = 2.51$) obtained here. Although the values are different due to the distinct high-energy band structures in various models, the differences are within 20%, implying the property of the low-energy Dirac dispersion dominates the critical interaction.

This relation has been proposed in previous studies on the uniform honeycomb-lattice and π-flux Hubbard models, [48,50], which is possible because the above two models have different velocities. In addition, this relation is confirmed in Ref. [52], where the Hubbard model with a d-wave pairing field allows the continuous tuning of the velocities. Here, the birefringent setup also allows a continuous tuning of the velocities, thus providing further understanding of the relationship between the critical interaction and the Dirac velocities. It is also noted that when the value of Δ_0 is large enough, the critical interaction can be well below the actual U value in graphene, resulting in the emergence of AFM order.

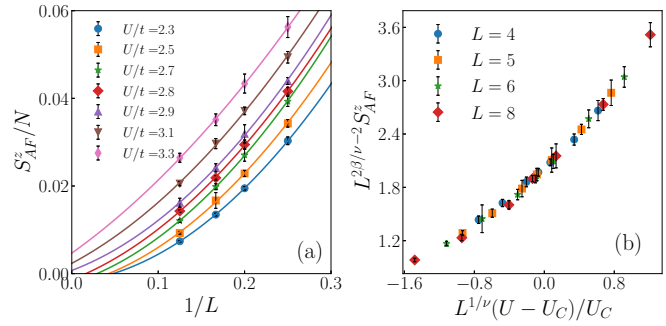

FIG. 5. (a) Extrapolation of the structure factor $S^z_{\rm AFM}/N$ near the transition point. The solid lines are least-squares fits to the polynomial form of $1/L$. The value in the thermodynamic limit becomes finite at some interaction between $U/t = 2.8$ and 2.9, thus the critical interaction is estimated to be $U_c/t = 2.85 \pm 0.05$. (b) The data collapse using the critical exponents of the Gross-Neveu-Heisenberg universality class and the critical interaction determined in (a). Here the anisotropic parameter is $\Delta_0/t = -0.3$.

We also perform a finite-size scaling analysis based on the usual scaling formula [47],

$$S^z_{\rm AFM} = L^{2-2\beta/\nu} F[L^{1/\nu}(U - U_c)], \tag{8}$$

where β is the order parameter exponent and ν is the correlation length exponent. The semimetal-AFM transition is expected to belong to the Gross-Neveu-Heisenberg universality class [53–56]. The previous DQMC studies reported $\nu = 1.02$ and $\beta = 0.76$ [48]. Together with the critical interaction determined by the finite-size scaling above, we scale $S^z_{\rm AFM}$ at different lattice sizes according to the above formula. As shown in Fig. 5(b), the data collapse is pretty good, thus confirming the universality class of the phase transition here is unchanged by the Y-shaped Kekulé distortion.

In addition, we have further checked the single-particle gap by extracting the spectral function and the density of states from the imaginary-time Green's function using analytic continuation (see Appendix B). It shows that the AFM transition is always accompanied by a charge-gap opening, indicating that the system becomes a AFM Mott insulator above U_c.

V. DISCUSSION

We have applied the mean-field theory and DQMC simulations to study the Hubbard model on a honeycomb lattice with a Y-shaped distortion. Both approaches reveal that AFM order develops above a critical interaction, and the critical interaction decreases monotonically with the distortion parameter and scales with the geometric average of the two velocities of the birefringent Dirac fermions. We find that the quantum criticality of the continuous AFM transition is unchanged by the distortion and still belongs to the Gross-Neveu-Heisenberg universality class.

The fact that the Y-shaped Kekulé distortion can continuously tune the quantum critical point is of great significance in graphene research and applications. When the critical point is put below the actual value of U in graphene [29,30], the long-sought bulk magnetism in graphene can be realized. Recent experiments [27,28] have demonstrated the realization of

Y-shaped distortion in graphene. For graphene on Cu(111), the distortion is likely due to regular copper vacancies which lead to a vertical shift of the central carbon atom of each Y-shaped texture [27]. Our result indicates that when the shift is large enough, AFM order should be spontaneously generated in the graphene layer. Thus, our results not only deepen our understanding of the semimetal-AFM transitions in Dirac fermion systems, but also provide a feasible approach to induce magnetism in graphene.

ACKNOWLEDGMENTS

C.W., W.H., and H.G. acknowledge support from the National Natural Science Foundation of China (NSFC) Grants No. 11774019 and No. 12074022, the NSAF grant in NSFC with Grant No. U1930402, the Fundamental Research Funds for the Central Universities and the HPC resources at Beihang University. X.F. and S.A.Y are supported by the Singapore MOE AcRF Tier 2 (MOE-T2EP50220-0011). S.F. is supported by the National Key Research and Development Program of China under Grant No. 2021YFA1401803, and NSFC under Grants No. 11974051 and No. 11734002.

APPENDIX A: THE BAND STRUCTURES AT VARIOUS VALUES OF Δ_0

In momentum space, the $U = 0$ Hamiltonian is given by

$$\mathcal{H}_0(\mathbf{k}) = \begin{pmatrix} 0 & h_{12}(\mathbf{k}) \\ h_{12}^{\dagger}(\mathbf{k}) & 0 \end{pmatrix}, \tag{A1}$$

where

$$h_{12}(\mathbf{k}) = -\begin{pmatrix} \Delta_- & \Delta_- e^{i\mathbf{k}\cdot\mathbf{a}_1} & \Delta_- \\ \Delta_- & \Delta_- & \Delta_- e^{i\mathbf{k}\cdot(\mathbf{a}_2-\mathbf{a}_1)} \\ \Delta_+ e^{i\mathbf{k}\cdot\mathbf{a}_2} & \Delta_+ & \Delta_+ \end{pmatrix}, \tag{A2}$$

with $\Delta_- = 1 - \Delta_0$, $\Delta_+ = 1 + 2\Delta_0$, and the lattice constants $\mathbf{a}_1 = 3(\sqrt{3}/2, -1/2)$, $\mathbf{a}_2 = 3(\sqrt{3}/2, 1/2)$. The whole spectrum has six dispersive bands, which can be obtained by directly diagonalizing the Hamiltonian in Eq. (1). The maximum value of the eigenenergy is at the Γ point, which is $6t\sqrt{2\Delta_0^2 + 1}$. Although the bandwidth varies with Δ_0, the way to parametrize the strong and weak bonds used in the main text minimizes the variation of the bandwidth as Δ_0 changes. Another advantage of this kind of choice is that the bandwidth is independent of the sign of Δ_0.

When Δ_0 varies from 0 to -0.5, the bandwidth of the two bands near the Fermi energy decreases continuously and becomes vanished at $\Delta_0/t = -0.5$ (see Fig. 6). The evolution of the bandwidth is similar in changing Δ_0 from 0 to 1. The difference is that the band-flatting process involves the four bands near the Fermi energy here.

1. The flat-band states at $\Delta_0/t = -0.5$

We have $\Delta_+ = 0$ at $\Delta_0/t = -0.5$, when the Hamiltonian in Eq. (1) can be solved analytically. Generally there are two zero-energy states at each momentum. As has been stated in the main text, one of them is totally localized on the fifth site, which is completely isolated from the lattice. The wave function of the other one

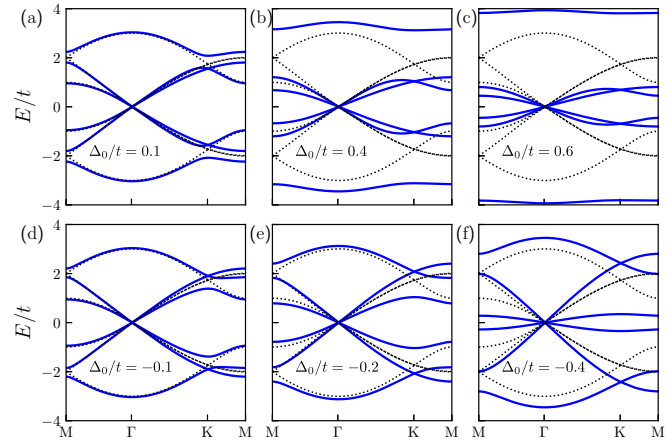

FIG. 6. The band structures at (a) $\Delta_0/t = 0.1$, (b) $\Delta_0/t = 0.4$, (c) $\Delta_0/t = 0.8$, (d) $\Delta_0/t = -0.1$, (e) $\Delta_0/t = -0.2$, (f) $\Delta_0/t = -0.4$. The dotted lines in each figure represent the band structure of graphene, i.e., the $\Delta_0/t = 0$ case, which are plotted for the purpose of comparison.

is $\psi_0(\mathbf{k}) = \lambda[0, 0, 0, f_1(\mathbf{k}), f_2(\mathbf{k}), 1]^T$, where $f_1(\mathbf{k}) = (1 - e^{i\mathbf{k}\cdot\mathbf{a}_2})/(e^{i\mathbf{k}\cdot\mathbf{a}_1} - 1)$, $f_2(\mathbf{k}) = [1 - e^{i\mathbf{k}\cdot(\mathbf{a}_2-\mathbf{a}_1)}]/(e^{i\mathbf{k}\cdot\mathbf{a}_1} - 1)$, and $\lambda = 1/\sqrt{1 + |f_1(\mathbf{k})|^2 + |f_2(\mathbf{k})|^2}$. Hence this flat-band state distributes only on the second, fourth, and sixth sites of the unit cell, each of which is connected by one red bond.

In real space, the above zero-energy states associated with the connected lattice can be constructed within each triple hexagon centered at the isolated site (see Fig. 8). Each such state only distributes on the six sites connected by two bonds. The weights among the sites are equal, and the phases of the wave function alternate between 1, -1 along the edge of the triple hexagon.

2. The flat-band states at $\Delta_0/t = 1$

At $\Delta_0/t = 1$, the lattice is decoupled into isolated sites and four-pointed stars. Four of the six eigenvalues at each $\mathbf{k}$ are zero-energy states. Two of them are completely localized on the isolated sites, and the other two are within the four-pointed

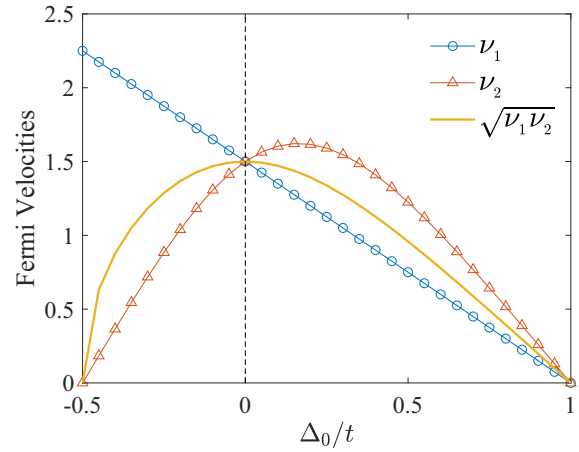

FIG. 7. The Fermi velocities ν_1, ν_2 and their geometric average $\sqrt{\nu_1\nu_2}$ as a function of Δ_0.

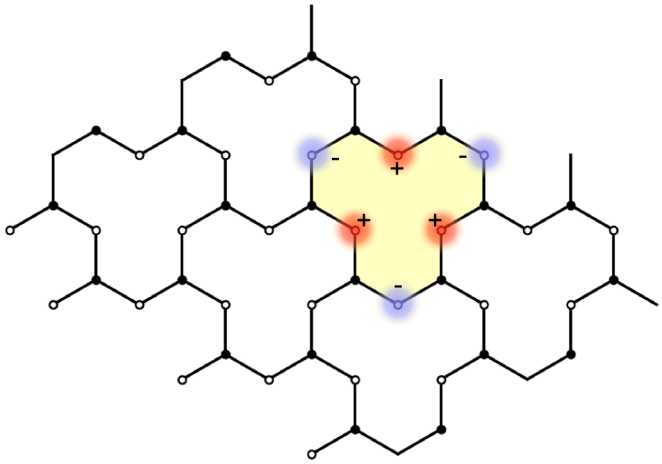

FIG. 8. The wave function of one of the flat-band states at $\Delta_0/t = -0.5$. Each such state is localized within the triple hexagon, and only distributes on the six sites connected by two bonds. The weights among the above sites are equal, and the phases of the wave function alternate between $1, -1$ along the edge of the triple hexagon.

stars, for which the Hamiltonian writes as

$$H = -t_+ \begin{pmatrix} 0 & 1 & 1 & 1 \\ 1 & 0 & 0 & 0 \\ 1 & 0 & 0 & 0 \\ 1 & 0 & 0 & 0 \end{pmatrix}. \tag{A3}$$

Its eigenvalues are $\pm\sqrt{3}t_+, 0, 0$. Two linearly independent eigenstates for the zero-energy states can be constructed as: $\psi_1 = \frac{1}{\sqrt{2}}[0, 1, -1, 0]^T$, $\psi_2 = \frac{1}{\sqrt{2}}[0, 1, 0, -1]^T$. The distributions of the above wave functions are only on the surrounding three sites, each of which is only connected by one bond.

3. Deducing of the low-energy effective Hamiltonian

At $\mathbf{k} = (0, 0)$, the eigenvectors corresponding to the four zero-energy states of the Dirac points forms the projection matrix:

$$P = \begin{pmatrix} 0 & 0 & -\frac{1}{\sqrt{2}} & \frac{-1-2\Delta_0}{\sqrt{-6+12\Delta_0^2}} \\ 0 & 0 & \frac{1}{\sqrt{2}} & \frac{-1-2\Delta_0}{\sqrt{-6+12\Delta_0^2}} \\ 0 & 0 & 0 & \frac{\sqrt{2}(1-\Delta_0)}{\sqrt{3+6\Delta_0}} \\ -\frac{1}{\sqrt{2}} & -\frac{1}{\sqrt{6}} & 0 & 0 \\ 0 & \sqrt{\frac{2}{3}} & 0 & 0 \\ \frac{1}{\sqrt{2}} & -\frac{1}{\sqrt{6}} & 0 & 0 \end{pmatrix}. \tag{A4}$$

Then the effective low-energy Hamiltonian is obtained by

$$H_{\text{eff}}(\mathbf{k}) = P^T \mathcal{H}_0(\mathbf{k}) P, \tag{A5}$$

which is

$$\mathcal{H}_{\text{eff}}(\mathbf{k}) = \begin{pmatrix} 0 & f(\mathbf{k}) \\ f^\dagger(\mathbf{k}) & 0 \end{pmatrix}, \tag{A6}$$

$$f(\mathbf{k}) = -\frac{3\mathbb{I}}{2}(1-\Delta_0)t \begin{pmatrix} k_y & \alpha k_x \\ -k_x & \alpha k_y \end{pmatrix}, \tag{A7}$$

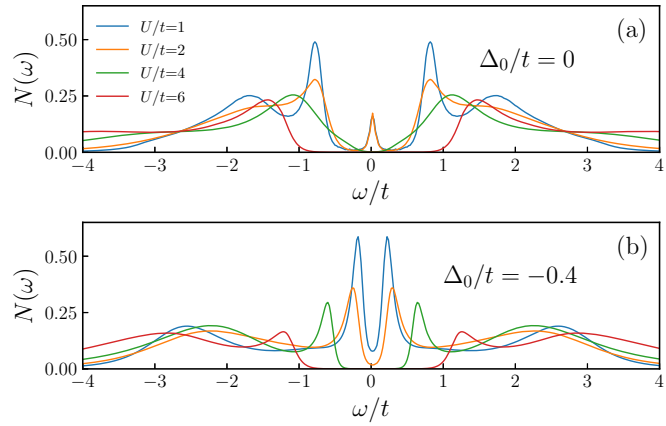

FIG. 9. The density of states $N(\omega)$ at various values of U: (a) $\Delta_0/t = 0$ and (b) $\Delta_0/t = -0.4$.

where the anisotropic factor is $\alpha = \frac{1+2\Delta_0}{\sqrt{1+2\Delta_0^2}}$.

APPENDIX B: THE SINGLE-PARTICLE EXCITATION

To investigate the single-particle gap, we use analytic continuation to extract the spectral function from the imaginary-time-dependent Green's function $G(\tau, \mathbf{k}) = \langle c_{\mathbf{k}}(\tau) c_{\mathbf{k}}^\dagger(0) \rangle$:

$$G(\tau, \mathbf{k}) = \frac{1}{\pi} \int_{-\infty}^{\infty} d\omega \frac{e^{-\tau\omega}}{1 + e^{-\beta\omega}} A(\mathbf{k}, \omega). \tag{B1}$$

Then the density of states, $N(\omega)$, can be directly calculated:

$$N(\omega) = \int dk A(k, \omega). \tag{B2}$$

$N(\omega)$ shown in Fig. 9 characterizes a metal-insulator transition driven by the Hubbard interaction U. The density of states is finite at $\omega = 0$ for small U. When U is large enough,

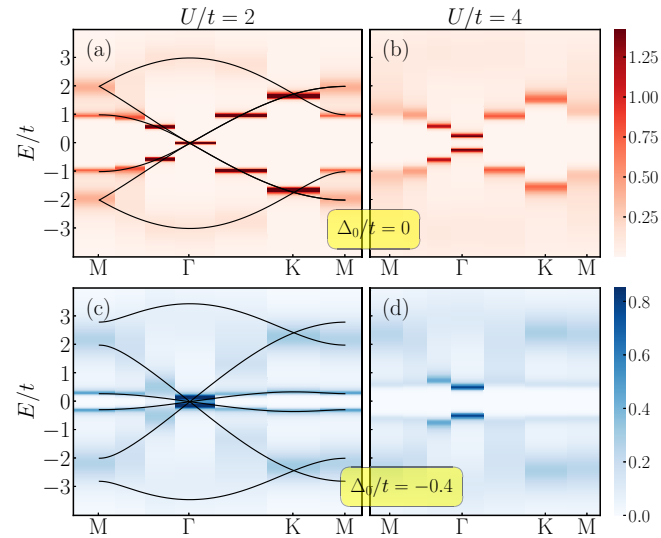

FIG. 10. The single-particle spectral function: (a) $\Delta_0/t = 0$, $U/t = 2$; (b) $\Delta_0/t = 0$, $U/t = 4$; (c) $\Delta_0/t = -0.4$, $U/t = 2$; (d) $\Delta_0/t = -0.4$, $U/t = 4$. Here the lattice size is $L = 6$ and the inverse temperature is $\beta = 20$.

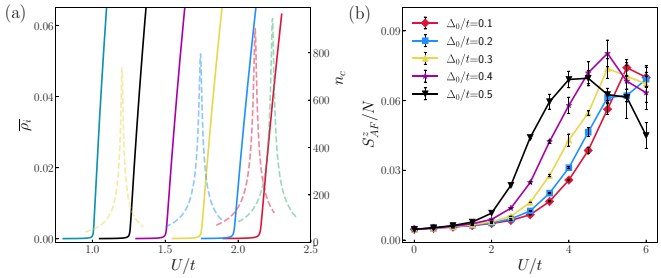

FIG. 11. (a) The mean-field order parameter and the cycling time n_c to get convergent solution in the self-consistent process as a function of U for various values of positive Δ_0. The sharp peak in the n_c curve can steadily determine the transition point. (b) The AFM structure factor obtained by DQMC as a function of U on a lattice with the size $L = 6$.

it is zero in a finite region near $\omega = 0$, which corresponds to the size of a charge gap. Compared to the $\Delta_0 = 0$ case, the gap opening occurs at smaller U for $\Delta_0 = -0.4$. The critical interactions estimated qualitatively are consistent with those determined from the AFM transition. This implies the AFM transition is accompanied by a charge-gap opening, suggesting the system is a AFM Mott insulator above the critical point.

The spectral function $A(\mathbf{k}, \omega)$ counts single-particle excitations at a given momentum and energy, thus allows us to locate the point in the Brillouin zone where the single-particle gap is minimum. As shown in Fig. 10, the gap is minimum at the Γ point, thus its opening occurs at the Dirac points.

APPENDIX C: THE SPIN CORRELATIONS

Figure 11(b) shows the AFM structure factor as a function of U for various values of positive Δ_0. For small Δ_0, S^z_{AFM}/N increases continuously with U, implying the existence of a continuous SM-AFM transition. In addition, as Δ_0 increases, the curves shift to the weak-interaction side, thus the critical interaction U_c should decrease as Δ_0 increases. The above behavior is consistent with the phase diagram of the main text. The case of $\Delta_0/t = 0.5$ is special, where S^z_{AFM}/N has a clear drop at sufficient large U. It should result from the collapse of the AFM order at strong U for large Δ_0, where an AFM to Y-dimer transition occurs.

Figure 12 plots the spin-spin correlation function between different kinds of pairs of sites as a function of Δ_0. The largest distance between the two sites in each kind of pair is considered, which can represent the long-range spin correlation. Figure 12(a) shows $c(\mathbf{r})$ in the region $\Delta_0 < 0$. The first, second, and fifth sites in each unit cell are connected by zero, one, and three weakened bonds, respectively. The values of the spin correlations have the following relation: $c_{5-5}(\mathbf{r}) > c_{2-2}(\mathbf{r}) > c_{1-1}(\mathbf{r})$. For $c(\mathbf{r})$ between the sites with different indexes, the relation of the corresponding values is $c_{2-5}(\mathbf{r}) > c_{1-5}(\mathbf{r}) > c_{1-2}(\mathbf{r})$. Hence, when the absolute value of Δ_0 is small, the value of $c(\mathbf{r})$ increases with the total number of weakened bonds connected to the two sites in each pair, which remains valid when all the values in Fig. 12(a) are compared. This suggests the spin correlation between two sites can be strengthened by locally weakening the bonds

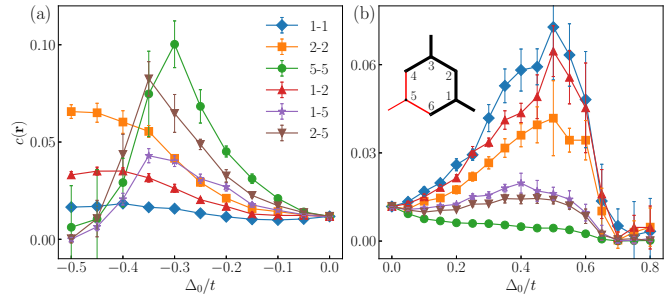

FIG. 12. The spin-spin correlations as a function of Δ_0 between the sites with the same and different indexes of the unit cells in the regions: (a) $\Delta_0 < 0$; (b) $\Delta_0 > 0$. Here $\mathbf{r}$ takes the largest distance in a $L = 6$ lattice, and the strength of the interaction is $U/t = 6$.

connecting them. As Δ_0 increases, the values of the spin correlations without the fifth index involved continuously increases and tends to constants in the $\Delta_0/t = -0.5$ limit. The sequence of the values keeps as $c_{2-2}(\mathbf{r}) > c_{2-1}(\mathbf{r}) > c_{1-1}(\mathbf{r})$. In contrast, the spin correlations involving the fifth site begin to decrease quickly from $\Delta_0/t \sim -0.3$, and becomes zero at $\Delta_0/t = -0.5$, which is expected since the fifth site is completely depleted from the lattice in this limit. As demonstrated in Fig. 12(b), the case with $\Delta_0 > 0$ is similar, except that all values begin to drop at $\Delta_0/t \sim 0.5$ and become zero at $\Delta_0/t \sim 0.7$. Here the vanishment of the spin correlations at extremely large Δ_0 is due to the occurrence of an AFM to Y-dimer transition.

In the large-U limit, the double occupancy is completely eliminated, and the Hubbard model in Eq. (1) maps onto the following Heisenberg model [57]:

$$\mathcal{H} = \sum_{\langle ij \rangle} J_{ij} \mathbf{S}_i \cdot \mathbf{S}_j, \tag{C1}$$

where the exchange coupling is $J_{ij} = \frac{4t_{ij}^2}{U}$. Corresponding to the Y-shaped modulations of the hopping amplitudes, the value of J_{ij} takes $J_1 = 4(1-\Delta_0)^2/U$ or $J_2 = 4(1+2\Delta_0)^2/U$. We set $J_1 = 1$ for $\Delta_0 < 0$ ($J_2 = 1$ for $\Delta_0 > 0$) as the energy scale, thus $J_2 = (1+2\Delta_0)^2/(1-\Delta_0)^2$ ($J_1 = (1-\Delta_0)^2/(1+2\Delta_0)^2$), which decreases monotonically as Δ_0 changes from 0 to $-0.5(1)$.

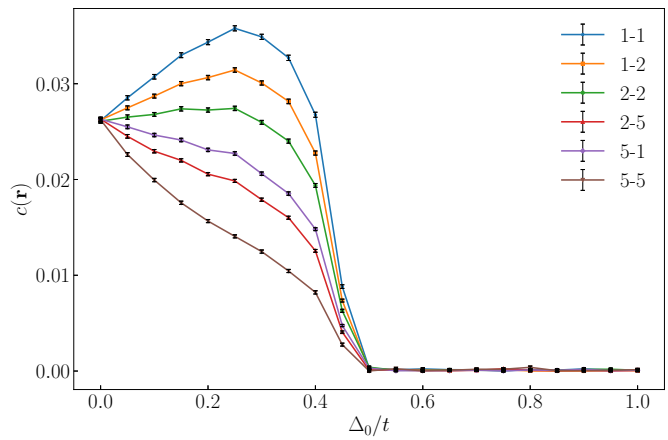

FIG. 13. The spin-spin correlations as a function of positive Δ_0 for the largest distance on a $L = 20$ lattice in the large-U limit.

Similar to the plot in Fig. 4(d) of the main text, we here plot the spin-spin correlations at the largest distance on a $L = 20$ lattice as a function of positive Δ_0 in the large-U limit in Fig. 13. Now the first, second, and fifth sites in each unit cell are connected by there, one, and zero weakened bonds, respectively. The values of the spin correlations have the following relation: $c_{1-1}(\mathbf{r}) > c_{1-2}(\mathbf{r}) > c_{2-2}(\mathbf{r}) > c_{5-1}(\mathbf{r}) > c_{2-5}(\mathbf{r}) > c_{5-5}(\mathbf{r})$. Hence, the statement that the value of $c(\mathbf{r})$ increases with the total number of weakened bonds connected to the two sites in each pair remains valid. Different from the case of $\Delta_0 < 0$, the value of $c(\mathbf{r})$ begins to be zero at $\Delta_0/t = 0.5$, where an AFM to Y-dimer transition occurs. Near the critical point, $c(\mathbf{r})$ decreases rapidly, implying the AFM order collapses quickly with increasing Δ_0 here.

[1] A. K. Geim and K. S. Novoselov, in *Nanoscience and Technology: A Collection of Reviews from Nature Journals* (World Scientific, Singapore, 2010), pp. 11–19

[2] A. H. Castro Neto, F. Guinea, N. M. R. Peres, K. S. Novoselov, and A. K. Geim, Rev. Mod. Phys. **81**, 109 (2009).

[3] K. S. Novoselov, A. K. Geim, S. V. Morozov, D. Jiang, M. I. Katsnelson, I. Grigorieva, S. Dubonos, and A. Firsov, Nature (London) **438**, 197 (2005).

[4] Y. Zhang, Y.-W. Tan, H. L. Stormer, and P. Kim, Nature (London) **438**, 201 (2005).

[5] M. Katsnelson, K. Novoselov, and A. Geim, Nat. Phys. **2**, 620 (2006).

[6] G. W. Semenoff, V. Semenoff, and F. Zhou, Phys. Rev. Lett. **101**, 087204 (2008).

[7] H.-M. Guo and M. Franz, Phys. Rev. B **80**, 113102 (2009).

[8] C. L. Kane and E. J. Mele, Phys. Rev. Lett. **95**, 226801 (2005).

[9] C.-Y. Hou, C. Chamon, and C. Mudry, Phys. Rev. Lett. **98**, 186809 (2007).

[10] C. Chamon, C.-Y. Hou, R. Jackiw, C. Mudry, S.-Y. Pi, and A. P. Schnyder, Phys. Rev. Lett. **100**, 110405 (2008).

[11] R. L. Frank and E. H. Lieb, Phys. Rev. Lett. **107**, 066801 (2011).

[12] C. Bao, H. Zhang, T. Zhang, X. Wu, L. Luo, S. Zhou, Q. Li, Y. Hou, W. Yao, L. Liu, P. Yu, J. Li, W. Duan, H. Yao, Y. Wang, and S. Zhou, Phys. Rev. Lett. **126**, 206804 (2021).

[13] M. Slota, A. Keerthi, W. K. Myers, E. Tretyakov, M. Baumgarten, A. Ardavan, H. Sadeghi, C. J. Lambert, A. Narita, K. Müllen *et al.*, Nature (London) **557**, 691 (2018).

[14] O. V. Yazyev and M. I. Katsnelson, Phys. Rev. Lett. **100**, 047209 (2008).

[15] J. Fernández-Rossier and J. J. Palacios, Phys. Rev. Lett. **99**, 177204 (2007).

[16] R. Babar and M. Kabir, Phys. Rev. B **99**, 115442 (2019).

[17] M. Kabir and T. Saha-Dasgupta, Phys. Rev. B **90**, 035403 (2014).

[18] O. V. Yazyev and L. Helm, Phys. Rev. B **75**, 125408 (2007).

[19] H. González-Herrero, J. M. Gómez-Rodríguez, P. Mallet, M. Moaied, J. J. Palacios, C. Salgado, M. M. Ugeda, J.-Y. Veuillen, F. Yndurain, and I. Brihuega, Science **352**, 437 (2016).

[20] O. V. Yazyev, Rep. Prog. Phys. **73**, 056501 (2010).

[21] A. Valli, A. Amaricci, A. Toschi, T. Saha-Dasgupta, K. Held, and M. Capone, Phys. Rev. B **94**, 245146 (2016).

[22] A. Valli, A. Amaricci, V. Brosco, and M. Capone, Phys. Rev. B **100**, 075118 (2019).

[23] W. Yao, S. A. Yang, and Q. Niu, Phys. Rev. Lett. **102**, 096801 (2009).

[24] M. Golor, T. C. Lang, and S. Wessel, Phys. Rev. B **87**, 155441 (2013).

[25] H. Feldner, Z. Y. Meng, T. C. Lang, F. F. Assaad, S. Wessel, and A. Honecker, Phys. Rev. Lett. **106**, 226401 (2011).

[26] H. Feldner, Z. Y. Meng, A. Honecker, D. Cabra, S. Wessel, and F. F. Assaad, Phys. Rev. B **81**, 115416 (2010).

[27] C. Gutiérrez, C.-J. Kim, L. Brown, T. Schiros, D. Nordlund, E. B. Lochocki, K. M. Shen, J. Park, and A. N. Pasupathy, Nat. Phys. **12**, 950 (2016).

[28] M.-H. Zhang, Y.-N. Ren, Q. Zheng, X.-F. Zhou, and L. He, Stabilizing sample-wide kekulé orders in graphene/transition metal dichalcogenide heterostructures, arXiv:2208.01286.

[29] Estimates for the graphene Hubbard U vary significantly in the literature. Here we use $U/t = 3.0$, which is obtained using the quantum chemistry Pariser-Parr-Pople method in Ref. [30].

[30] H.-K. Tang, J. Leaw, J. Rodrigues, I. Herbut, P. Sengupta, F. Assaad, and S. Adam, Science **361**, 570 (2018).

[31] E. H. Lieb, Phys. Rev. Lett. **62**, 1201 (1989).

[32] Y. Huang, H. Guo, J. Maciejko, R. T. Scalettar, and S. Feng, Phys. Rev. B **102**, 155152 (2020).

[33] H.-M. Guo, L. Wang, and R. T. Scalettar, Phys. Rev. B **97**, 235152 (2018).

[34] X. Zhu, H. Guo, and S. Feng, J. Phys.: Condens. Matter **31**, 505601 (2019).

[35] S. Sorella and E. Tosatti, Europhys. Lett. **19**, 699 (1992).

[36] R. Blankenbecler, D. J. Scalapino, and R. L. Sugar, Phys. Rev. D **24**, 2278 (1981).

[37] J. E. Hirsch, Phys. Rev. Lett. **51**, 1900 (1983).

[38] J. E. Hirsch, Phys. Rev. B **31**, 4403 (1985).

[39] S. R. White, D. J. Scalapino, R. L. Sugar, E. Y. Loh, J. E. Gubernatis, and R. T. Scalettar, Phys. Rev. B **40**, 506 (1989).

[40] E. Y. Loh, J. E. Gubernatis, R. T. Scalettar, S. R. White, D. J. Scalapino, and R. L. Sugar, Phys. Rev. B **41**, 9301 (1990).

[41] M. Troyer and U.-J. Wiese, Phys. Rev. Lett. **94**, 170201 (2005).

[42] V. I. Iglovikov, E. Khatami, and R. T. Scalettar, Phys. Rev. B **92**, 045110 (2015).

[43] Z.-X. Li, Y.-F. Jiang, and H. Yao, Phys. Rev. B **91**, 241117(R) (2015).

[44] C. N. Varney, C.-R. Lee, Z. J. Bai, S. Chiesa, M. Jarrell, and R. T. Scalettar, Phys. Rev. B **80**, 075116 (2009).

[45] Z. Meng, T. Lang, S. Wessel, F. Assaad, and A. Muramatsu, Nature (London) **464**, 847 (2010).

[46] S. Sorella, Y. Otsuka, and S. Yunoki, Sci. Rep. **2**, 992 (2012).

[47] F. F. Assaad and I. F. Herbut, Phys. Rev. X **3**, 031010 (2013).

[48] Y. Otsuka, S. Yunoki, and S. Sorella, Phys. Rev. X **6**, 011029 (2016).

[49] T. Paiva, R. T. Scalettar, W. Zheng, R. R. P. Singh, and J. Oitmaa, Phys. Rev. B **72**, 085123 (2005).

[50] F. Parisen Toldin, M. Hohenadler, F. F. Assaad, and I. F. Herbut, Phys. Rev. B **91**, 165108 (2015).

[51] J. Ostmeyer, E. Berkowitz, S. Krieg, T. A. Lähde, T. Luu, and C. Urbach, Phys. Rev. B **104**, 155142 (2021).
[52] Y. Otsuka, K. Seki, S. Sorella, and S. Yunoki, Phys. Rev. B **102**, 235105 (2020).
[53] I. F. Herbut, Phys. Rev. Lett. **97**, 146401 (2006).
[54] I. F. Herbut, V. Juričić, and B. Roy, Phys. Rev. B **79**, 085116 (2009).
[55] B. Roy, M. P. Kennett, K. Yang, and V. Juričić, Phys. Rev. Lett. **121**, 157602 (2018).
[56] B. Roy and V. Juričić, Phys. Rev. Res. **2**, 012047(R) (2020).
[57] C. L. Cleveland and R. Medina A., Am. J. Phys. **44**, 44 (1976).